

Quantum Supercriticality in the Ising Model and Rydberg Atom Array

Junsen Wang,^{1,2} Enze Lv,^{2,3} Xinyang Li,^{2,3} Yuliang Jin,^{2,3,*} and Wei Li^{2,3,†}

¹Center of Materials Science and Optoelectronics Engineering,
College of Materials Science and Opto-electronic Technology,

University of Chinese Academy of Sciences, Beijing 100049, China

²Institute of Theoretical Physics, Chinese Academy of Sciences, Beijing 100190, China

³School of Physical Sciences, University of Chinese Academy of Sciences, Beijing 100049, China

(Dated: July 9, 2024)

Supercriticality, featured with universal scaling behaviors, emerges as an intriguing phenomenon proximate to the classical liquid-gas critical point. In this study, we extend this significant concept to quantum many-body systems near the quantum critical point (QCP), employing tensor network calculations and scaling analyses of the Ising model and Rydberg atom array. The supercritical, fluid-like, quantum states are found to be strongly fluctuating and highly entangled, as characterized by the universal scalings in susceptibility $\chi_z \sim (h_x - h_x^c)^{-\gamma}$, correlation length $\xi \sim (h_x - h_x^c)^{-\nu}$, fidelity susceptibility $\chi_F \sim (h_x - h_x^c)^{d\nu-2}$, and entanglement entropy $S_E \sim \ln(h_x - h_x^c)$. Here, γ and ν represent critical exponents, d is the dimension of the system, and h_x^c is the critical transverse field of the Ising QCP. The universal scaling behaviors are revealed in the regime enclosed by two quantum supercritical crossover lines in the longitudinal-transverse field (h_z - h_x) plane, $|h_z| \propto (h_x - h_x^c)^{\beta+\gamma}$ relating to critical exponents β and γ , where the response functions, measures of entanglement, and fidelity susceptibility reach their maxima. We propose that Rydberg atom arrays and quantum Ising magnets provide available platforms for exploring emergent supercritical phenomena and identifying the universal scalings. The present work establishes a foundation for exploring quantum supercriticality in magnetic systems and through quantum simulations.

Introduction.— Supercritical fluids do not show a distinct phase transition and instead display continuous crossovers marked by gradual property changes, above the liquid-gas critical point. Despite this, supercritical crossover lines exist, separating different asymptotic regimes, and have been extensively studied before. Prominent among these are the Fisher-Widom line based on the radical distribution function [1–7], the Widom line defined as the locus of maximum correlation length as well as thermodynamic response functions [8–19], the Frenkel line that involves the kinetic theory of liquids [20–29], and the recently proposed two symmetric supercritical crossover lines with a universal scaling [30].

Beyond classical fluids, the concept of supercriticality has been applied to study strongly correlated electrons, like the pseudogap temperature T^* in high- T_c superconductors [31–34]; and to explore the interacting matter described by quantum chromodynamics, where the existence of a putative critical point in the phase diagram [35–37] implies the existence of a Widom line [38]. To date, studies of supercritical phenomena have mainly concentrated on the regimes near the finite-temperature critical point.

Supercriticality emerges from the critical point at the end of a first-order transition line, characterized by strong thermal fluctuations (c.f., Fig. 1). On the other hand, it has been acknowledged that a similar situation, namely, the first-order line concluding at a quantum critical point (QCP) [39–41] is also present in the *quantum phase diagram*. A prominent example is the quantum Ising model with both transverse (h_x) and longitudinal (h_z) fields. This prompts intriguing questions: can we identify a quantum supercritical (QSC) regime beyond the QCP? Furthermore, what characteristics and crossover lines define the QSC regime, if it exists?

In this work, we carry out systematic studies of QSC

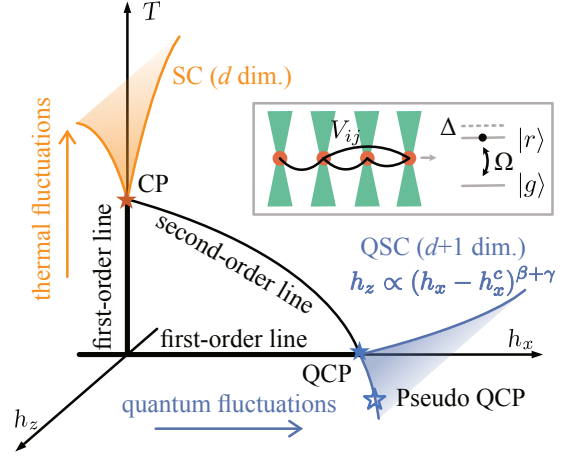


FIG. 1. Schematic phase diagram of the d -dimensional quantum Ising model with both transverse (h_x) and longitudinal (h_z) fields. In the T - h_z plane, there is a classical supercritical regime above the thermal critical point; and in the h_x - h_z plane, a QSC regime emerges. The QSC crossover line contains pseudo QCPs marked by the hollow star, which follows the universal scaling $h_z \propto (h_x - h_x^c)^{\beta+\gamma}$. The inset illustrates the Rydberg atom array described by Eq. (2), an ideal platform for investigating the QSC phenomena.

crossovers in the paradigmatic quantum Ising model and propose its simulations with the Rydberg atom array. Our main conclusion is summarized in Fig. 1, where we extend the concept of supercriticality from thermal phase transition in the h_z - T plane to the quantum phase transitions in the h_z - h_x plane. From the maximal of response functions and quantum information characteristics, we determine two QSC crossover lines with the universal scaling $|h_z| \propto (h_x - h_x^c)^{\beta+\gamma}$, which

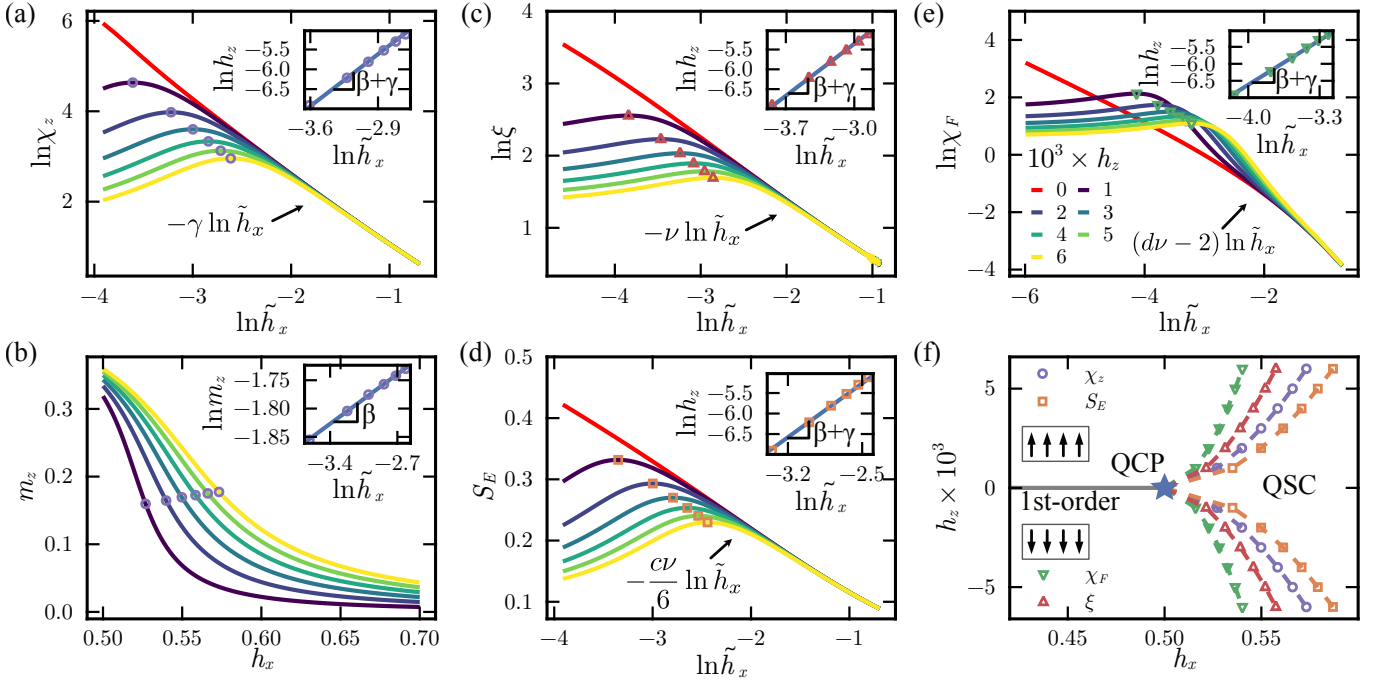


FIG. 2. (a) shows the behaviors of magnetic susceptibility under various fields h_z . In the inset, we plot the peaks (purple hollow circle) obtained from each curve, and find a power-law scaling $h_z \propto \tilde{h}_x^{\beta+\gamma}$ as given by the blue line. (b) shows the behaviors of the magnetization M_z on the crossover line as determined in (a), with a universal scaling $m_z \propto \tilde{h}_x^\beta$ revealed in the inset. The behaviors of (c) correlation length ξ , (d) entanglement entropy S_E , and (e) fidelity susceptibility χ_F are also plotted, with the determined QSC crossover lines shown in the insets. (f) The first-order line separates the spin-up and spin-down phases, and the spin up-down indistinguishable, i.e., quantum disordered regime is enclosed by the two crossover lines determined from various measurements χ_z , ξ , S_E , and χ_F .

enclose a QSC regime featuring prominent quantum fluctuations and entanglement with power-law scalings. Furthermore, we propose that the Rydberg atom array (c.f., inset of Fig. 1) offer an ideal platform for exploring the QSC regime and related scalings. We also discuss the relevance and implications of QSC crossovers and pseudo QCPs in Ising magnets such as CoNb_2O_6 [42–47].

Quantum Ising model with transverse and longitudinal fields.— As the most paradigmatic example, we consider the quantum Ising model with Hamiltonian

$$H = -J \sum_{\langle i,j \rangle} S_i^z S_j^z - h_x \sum_i S_i^x - h_z \sum_i S_i^z, \quad (1)$$

where $J \equiv 1$ is set as the energy scale (meaning ferromagnetic, FM case), and $h_{x(z)}$ is the transverse (longitudinal) field. In order to explore the QSC states, we examine the one-dimensional (1D) Ising model; however, it should be noted that the conclusions drawn are equally applicable to 2D and even higher-dimensional lattices (e.g., Fig. 1). In 1D quantum Ising chain, there is a QCP at $h_x = h_x^c \equiv 0.5$ for $h_z = 0$, and we define $\tilde{h}_x = h_x - h_x^c$. A small longitudinal field h_z smoothens the QCP, yet a QSC regime still emerges above it, as detailed subsequently.

For zero-temperature studies, we use a matrix product state approach [48] to calculate various ground-state properties of the quantum Ising model, with a fixed maximal bond dimen-

sion $D = 256$. We also consider the finite-temperature properties of this model, where the linearized tensor renormalization group algorithm [49, 50] is employed to calculate thermodynamic quantities like the magnetic specific heat. There we also fix the maximal bond dimension as $D = 256$, which renders the very well converged results.

Universal QSC scalings and crossovers.— In Fig. 2(a) we first show the magnetic susceptibility $\chi_z(h_x) \equiv \frac{\partial m_z}{\partial h_z}$ for various h_z . The red line, corresponding to $h_z = 0$, shows a critical scaling $\chi_z \propto \tilde{h}_x^{-\gamma}$ with $\gamma = 7/4$. All curves with different longitudinal h_z fields initially follow the universal scaling, but eventually deviate by reaching a maximal value and then decreasing, as h_x approaching h_x^c . Moreover, the peaks of the curve becomes lowered and more broadened as h_z increases, shifting to a greater h_x value. According to the quantum-classical mapping [40], χ_z is analogous to the magnetic susceptibility in the 2D classical Ising model. This correspondence suggests that the QSC crossover line can be determined by identifying peaks in the χ_z curves [30], marked as purple hollow circle in Fig. 2(a). Furthermore, the inset demonstrates that these peaks adhere to a power-law scaling $h_z \propto \tilde{h}_x^{\beta+\gamma}$ with $\beta + \gamma = 15/8$ from Ising universality class. Along this QSC crossover line, we further reveal that the magnetization $m_z \propto \tilde{h}_x^\beta$ with $\beta = 1/8$ [see Fig. 2(b)]. In Fig. 2(c), we show the correlation length ξ extracted from the spin-spin correlation function $\langle S_i^z S_{i+r}^z \rangle \propto e^{-r/\xi}$. Various curves un-

der different h_z initially all follow a universal scaling $\xi \propto \tilde{h}_x^{-\nu}$ with $\nu = 1$ [41], while eventually deviate by reaching a maximal value and then dropping, as h_x approaches h_x^c . This again renders a QSC crossover line $h_z \propto \tilde{h}_x^{\beta+\gamma}$ as shown in the inset of Fig. 2(c).

We then move on to the bipartite entanglement entropy S_E and fidelity susceptibility χ_F [51]. In Fig. 2(d), S_E curves are plotted for various h_z , following the scaling $S_E \sim -\frac{c\nu}{6} \log_2 \tilde{h}_x$, where $c = 1/2$ denotes the conformal central charge [52]. Regarding the fidelity susceptibility χ_F , we view Eq. (1) as a one-parameter (h_x) family of Hamiltonian: $H(h_x) = H_0 + h_x H_1$, where $H_0 = -J \sum_{\langle i,j \rangle} S_i^z S_j^z - h_z \sum_i S_i^z$ and $H_1 = -\sum_i S_i^x$. The quantum fidelity is defined as $F(h_x, \epsilon) = |\langle \psi_0(h_x) | \psi_0(h_x + \epsilon) \rangle|$, where $|\psi_0(h_x)\rangle$ denotes the ground state under a transverse field h_x . The fidelity susceptibility $\chi_F(h_x) = \partial^2 F(h_x, \epsilon) / \partial \epsilon^2 |_{\epsilon=0}$ is plotted for various h_z in Fig. 2(e), where we find universal scaling $\chi_F \propto \tilde{h}_x^{d\nu-2}$ [53] in the QSC regime. For nonzero h_z , we find that both S_E and χ_F initially adheres to these universal scalings, then peaks and declines as h_x approaches h_x^c . In the insets of Fig. 2(d) and (e), we show the QSC crossover lines determined from peaks of these quantum information characteristics, which again follow the universal power-law scaling. In summary, Fig. 2(f) displays the four QSC crossover lines determined, establishing a phase diagram containing spin-up (“liquid”), spin-down (“gas”), and the up-down indistinguishable (supercritical “fluid”) regimes. Despite differences among the lines derived from various quantities, they all follow the same $h_z \propto \tilde{h}_x^{\beta+\gamma}$ scaling relation.

Derivation of the QSC scalings.— The universal QSC behaviors depicted in Fig. 2 can be comprehended through scaling analysis [41]. In the vicinity of a QCP, the singular part of ground-state energy reads $\mathcal{U} = \tilde{h}_x^{2-\alpha} \phi_E(h_z/\tilde{h}_x^{\beta+\gamma})$, where $\phi_E(x)$ is the scaling function with $x \equiv h_z/\tilde{h}_x^{\beta+\gamma}$. We then have the singular part of magnetization $\mathcal{M}_z = \tilde{h}_x^\beta \phi_{m_z}(x)$ and susceptibility $\mathcal{X}_z = \tilde{h}_x^{-\gamma} \phi_{\chi_z}(x) = \tilde{h}_z^{-\beta+\gamma} \tilde{\phi}_{\chi_z}(x)$, where $\tilde{\phi}_{\chi_z}(x) \equiv x^{\beta+\gamma} \phi_{\chi_z}(x)$ and the Rushbrooke relation $\alpha + 2\beta + \gamma = 2$ is used. Therefore, the condition $\frac{\partial \mathcal{X}_z}{\partial h_x} = 0$ for the peaks observed in Fig. 2(a) is equivalent to finding the peak position where $\tilde{\phi}'_{\chi_z}(x_0) = 0$. In Fig. 3(a), we obtain the scaling function $\tilde{\phi}_{\chi_z}(x)$ via data collapse (see more details in SM [54]), and the QSC crossover is indeed positioned at x_0 , aligning precisely with the QSC crossover identified in Fig. 2. As $\phi_{\chi_z}(x)$ is an analytical and parity even function, we can expand it as $\phi_{\chi_z}(x) = \phi_{\chi_z}(0) + \frac{1}{2} \phi''_{\chi_z}(0) x^2 + \mathcal{O}(x^4)$, and find $\phi_{\chi_z}(x) \approx \phi_{\chi_z}(0)$, i.e., a constant, within the QSC regime [c.f., Fig. 3(b)]. This well explains the observed scaling $\chi_z \propto \tilde{h}_x^{-\gamma}$ seen in Fig. 2(a). It demonstrates that the universal scaling behaviors and QSC crossover lines are exclusively determined by the analytical properties of the scaling functions. Similarly, other universal scalings and supercritical crossovers of different quantities, such as correlation length ξ , entanglement entropy S_E and fidelity susceptibility χ_F , can be similarly derived [54].

Quantum simulations with Rydberg atom arrays.— Re-

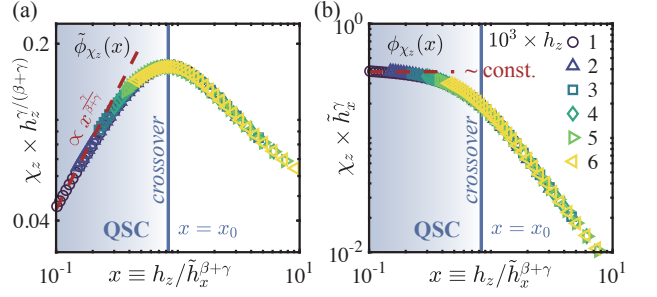


FIG. 3. Universal scaling functions (a) $\tilde{\phi}_{\chi_z}(x)$ and (b) $\phi_{\chi_z}(x)$ of the magnetic susceptibility χ_z near the Ising QCP. The $x = x_0$ vertical line obtained from Fig. 2(a) marks the QSC crossover, where $\tilde{\phi}'_{\chi_z}(x_0) = 0$.

cently, the Rydberg atom array has emerged as an ideal platform simulating and exploring exotic quantum phases of matter [55–64]. Notably, the quantum Ising model with tunable interaction has been realized with trapped cold atoms in 1D [55, 60] and 2D lattices [58, 63, 64]. It thus raises an intriguing question of whether the QSC phenomena and universal scalings can be simulated with Rydberg atom arrays.

We consider the following many-body Hamiltonian for the 1D Rydberg atom array [65–68]

$$H_{\text{Ryd}} = \frac{\Omega}{2} \sum_i \sigma_i^x - \Delta \sum_i n_i + \sum_{i < j} V_{ij} n_i n_j, \quad (2)$$

where Ω is the Rabi frequency that characterizes the coupling between ground state $|g_i\rangle$ and Rydberg state $|r_i\rangle$ with n_i being the corresponding Rydberg state number, Δ is the laser detuning (see inset in Fig. 1), and $V_{ij} = \frac{C_6}{(a|i-j|)^6}$ is the van der Waals interaction. $|C_6/a^6| \equiv 1$ is set as the energy unit, with C_6 the coupling coefficient and a the nearest-neighbor distance. The remarkable tunability of Rydberg atom arrays allows us to consider the attractive case with $C_6 < 0$, which corresponds to the FM Ising case.

We calculate the ground state using density-matrix renormalization group method [69–71] with system size $L = 256$ and truncated V_{ij} up to the fifth neighboring sites. We fix the maximal bond dimension $D = 500$ with truncation error smaller than 10^{-7} . The mean Rydberg excitation density $n = \sum_i \langle n_i \rangle / L$ is calculated in Fig. 4(a), which is the order parameter distinguishing the Rydberg atom “gas” (small n) and “liquid” phases. In Fig. 4(b,c), we plot the contours of compressibility $\kappa \equiv \frac{\partial n}{\partial \Delta}$ and entanglement entropy S_E , which highlight the QSC regime with prominent density fluctuations and quantum entanglement. The crossover lines are identified by the peaks of κ and S_E , which fall into the power-law scalings of Ising universality class as shown in Fig. 4(d).

The Rydberg atom array in Eq. (2) can be associated with an FM Ising system of pseudo-spins [65–68] $H = \Omega \sum_i S_i^x + \left(-\Delta - \zeta(6) \frac{|C_6|}{a^6}\right) \sum_i S_i^z + \sum_{ij} V_{ij} S_i^z S_j^z$, via the mapping $|g_i\rangle \rightarrow |\downarrow_i\rangle$, $|r_i\rangle \rightarrow |\uparrow_i\rangle$, $n_i = |r_i\rangle\langle r_i| \rightarrow \frac{1}{2} + S_i^z$,

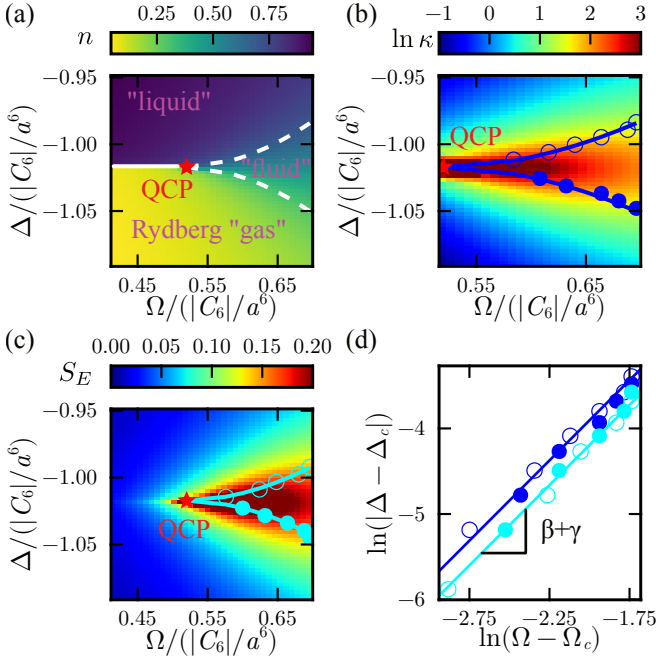


FIG. 4. The contour plots of (a) density n , (b) compressibility κ , and (c) entanglement entropy in the Δ - Ω plane. The blue solid and hollow circles in (b) are identified from peaks of κ , while the cyan solid and hollow circles in (c) represent peaks of S_E . Both are obtained by scanning Ω with various fixed Δ . (d) displays the QSC crossover lines discerned from κ and S_E , both of which adhere to the scaling $(\Delta - \Delta_c) \sim (\Omega - \Omega_c)^{\beta+\gamma}$, with $\Delta_c \approx -1.02$ and $\Omega_c \approx 0.52$ is location of QCP determined from panel (c).

where $\zeta(s) = \sum_{k=1}^{\infty} \frac{1}{k^s}$ is the Riemann zeta function with $\zeta(6) \approx 1.02$. Since the long-range FM spin couplings decay algebraically as $1/r^\alpha$ with an exponent $\alpha = 6 > 3$, the related QCP falls into the 1+1D Ising universality class [72–75]. We advocate that the Rydberg atom array thus offers an ideal platform for investigating the supercritical phenomena with universal scalings.

Pseudo QCP at the crossover line.— Quantum critical fan is an extended low-temperature regime above the QCP [39–41, 76, 77]. In Fig. 5(a), we display the contour plots of $\partial^2 C_m / \partial h_x^2$, and find a very prominent quantum critical fan characterized by two linear (as $z\nu = 1$) boundaries emanating from the QCP. In contrast, in Fig. 5(b) under small h_z , these two lines of white dots converge smoothly at low temperatures, suggesting that a pseudo QCP exists at the minimal position with $h_x^* = 0.54$.

In Fig. 5(c,d) plot the C_m/T data for the $h_z = 0$ and $h_z = 0.003$ cases, respectively. For $h_z = 0.0$ and near the QCP, C_m/T is a constant at low temperatures, as highlighted by the line with $h_x^c = 0.5$. However, for $h_z = 0.003$, there is only a limited temperature window for nearly constant C_m/T before it eventually drops. Since multiple curves lie within the gray band in Fig. 5(d), we determine the pseudo QCP h_x^* with error bar as shown in the inset of Fig. 5(d). It is noteworthy that the pseudo QCPs constitute a QSC crossover line, i.e.,

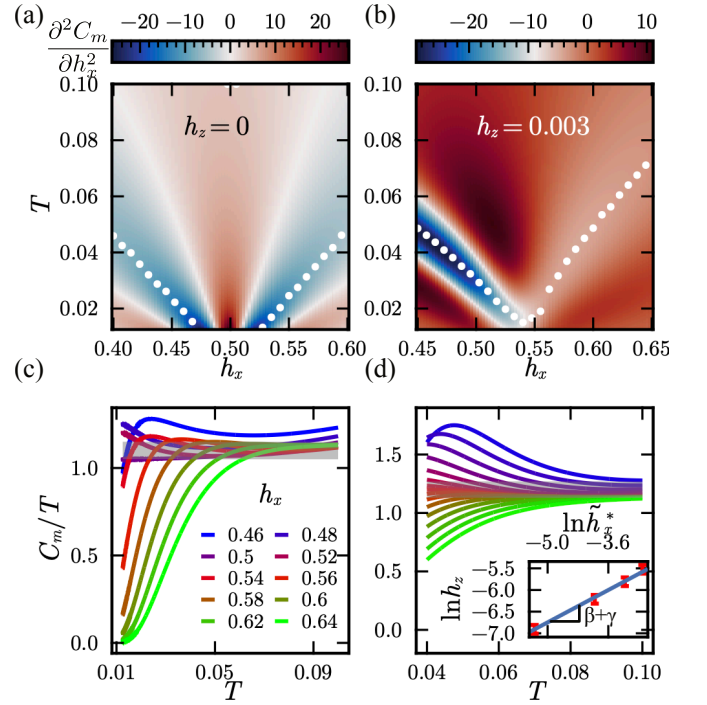


FIG. 5. (a) and (b) show the contour of $\partial^2 C_m / \partial h_x^2$ and C_m/T vs. T under $h_z = 0$. (b) and (d) show the same quantities but under $h_z = 0.003$. From (c) one can determine the location of QCP as $h_x^c = 0.5$, and in (d) the pseudo QCP h_x^* deviates from h_x^c under a finite h_z . The inset in (d) shows that the scaling $h_z \propto \tilde{h}_x^{\beta+\gamma}$ of the pseudo QCPs.

$h_z \propto \tilde{h}_x^{\beta+\gamma}$, where $\tilde{h}_x \equiv h_x^* - h_x^c$.

Such pseudo QCPs associated with the QSC scalings may offer insights for understanding experiments in quantum Ising chains and related materials. Recent studies on the Ising chain materials, such as CoNb_2O_6 [42–45, 47, 78–84], $\text{BaCo}_2\text{V}_2\text{O}_8$ [46, 85–88], and $\text{SrCo}_2\text{V}_2\text{O}_8$ [89–91], reveal that these materials are characterized by inter-chain couplings that are significantly weaker than the intra-chain couplings. A ‘hidden’ 1D QCP (h_c^{1D*}) within the 3D ordered phase of the coupled Ising chains has been proposed. However, the exact position of h_c^{1D*} for, say CoNb_2O_6 , varies with the measurement techniques: $h_c^{1D*} \simeq 5.25$ T by NMR [43], $h_c^{1D*} \simeq 5$ T by neutron scattering [42], $h_c^{1D*} \simeq 4.75$ T through terahertz spectroscopy [81], and $h_c^{1D*} \simeq 4.6$ -5.2 T from specific heat measurements [45].

With our QSC theory, these discrepancies can be comprehended. At the mean-field level, the interchain coupling can induce a weak longitudinal field on the Ising chains [92, 93]. Considering an interchain coupling of roughly $J_{\text{inter}}/J \sim \mathcal{O}(0.01)$ in CoNb_2O_6 [84], the effective longitudinal field is estimated as $h_z^{\text{eff}} = J_{\text{inter}} \langle S_i^z \rangle \sim 10^{-3} J$ (assuming $\langle S_i^z \rangle \sim \mathcal{O}(0.1)$). This indeed permits the occurrence of QSC phenomena in the compound. Consequently, h_c^{1D*} actually represents a pseudo QCP located at the QSC crossover line. Since different physical quantities may correspond to different crossover

lines [cf. Fig. 2(f)], the estimated h_c^{1D*} vary depending on the specific quantity under examination.

Summary and outlook.— The longitudinal field h_z triggers a first-order transition in the symmetry-breaking phase, and induces an extended regime beyond the QCP. These fluid-like supercritical quantum states, characterized by strong fluctuations and high entanglement, are bounded by crossover lines with universal power-law scaling. The quantum-classical mapping illuminates this scaling in various response functions, and we discover that entanglement and fidelity can also be utilized to study supercriticality in the quantum realm. The emergent QSC regime, characterized by the crossover scalings, is explained by analyzing the associated universal functions.

The profound link between liquid-gas and ferromagnetic transitions has been essential for understanding universality in the critical phenomena. Our research establishes the foundation for studying the quantum analogue of supercritical fluids and calls for further experimental studies. Now that cold neutral atoms can form Rydberg “liquid” and “gas” states, corresponding to the up and down spin states, we have a unique opportunity to investigate the Rydberg supercritical “fluid”. Recently, there has been substantial interest in simulating universal behaviors and obtaining critical exponents using Rydberg atom arrays [58, 60, 61]. We demonstrate that the supercritical crossover lines exhibit very robust scaling not confined to the immediate vicinity of the QCP, making them more detectable even with a moderately-sized Rydberg atom array [57, 59, 94].

Acknowledgments.— J.W. and W.L. are indebted to Ning Xi, Guoliang Wu, Lei-Yi-Nan Liu and Jian Cui for stimulating discussions. This work was supported by the National Natural Science Foundation of China (Grant Nos. 12222412 and 12047503), the Fundamental Research Funds for the Central Universities, and the CAS Project for Young Scientists in Basic Research (YSBR-057). We thank the HPC-ITP for the technical support and generous allocation of CPU time.

* yuliangjin@mail.itp.ac.cn

† w.li@itp.ac.cn

- [1] M. E. Fisher and B. Widom, Decay of correlations in linear systems, *J. Chem. Phys.* **50**, 3756 (1969).
- [2] R. J. F. L. d. Carvalho, R. Evans, D. C. Hoyle, and J. R. Henderson, The decay of the pair correlation function in simple fluids: long- versus short-ranged potentials, *J. Phys. Condens. Matter* **6**, 9275 (1994).
- [3] C. Vega, L. F. Rull, and S. Lago, Location of the Fisher-Widom line for systems interacting through short-ranged potentials, *Phys. Rev. E* **51**, 3146 (1995).
- [4] M. Dijkstra and R. Evans, A simulation study of the decay of the pair correlation function in simple fluids, *The Journal of Chemical Physics* **112**, 1449 (2000).
- [5] R. Evans, J. R. Henderson, D. C. Hoyle, A. O. Parry, and Z. A. Sabeur, Asymptotic decay of liquid structure: oscillatory liquid-vapour density profiles and the Fisher-Widom line, *Molecular Physics* **80**, 755 (1993).
- [6] P. TARAZONA, E. CHACÓN, and E. VELASCO, The Fisher-Widom line for systems with low melting temperature, *Molecular Physics* **101**, 1595 (2003).
- [7] D. Stopper, H. Hansen-Goos, R. Roth, and R. Evans, On the decay of the pair correlation function and the line of vanishing excess isothermal compressibility in simple fluids, *J. Chem. Phys.* **151**, 10.1063/1.5110044 (2019).
- [8] C. Domb and M. S. Green, eds., *Phase Transitions and Critical Phenomena*, Vol. 2 (Academic, New York, 1972).
- [9] L. Xu, P. Kumar, S. V. Buldyrev, S.-H. Chen, P. H. Poole, F. Sciortino, and H. E. Stanley, Relation between the Widom line and the dynamic crossover in systems with a liquid–liquid phase transition, *Proc. Natl. Acad. Sci.* **102**, 16558 (2005).
- [10] G. O. Jones and P. A. Walker, Specific heats of fluid Argon near the critical point, *Proc. Phys. Soc. London, Sect. B* **69**, 1348 (1956).
- [11] V. V. Brazhkin, Y. D. Fomin, A. G. Lyapin, V. N. Ryzhov, and E. N. Tsiok, Widom line for the liquid–gas transition in Lennard-Jones system, *The Journal of Physical Chemistry B* **115**, 14112 (2011).
- [12] G. Ruppeiner, A. Sahay, T. Sarkar, and G. Sengupta, Thermodynamic geometry, phase transitions, and the Widom line, *Phys. Rev. E* **86**, 052103 (2012).
- [13] D. T. Banuti, Crossing the Widom-line – supercritical pseudo-boiling, *The Journal of Supercritical Fluids* **98**, 12 (2015).
- [14] H.-O. May and P. Mausbach, Riemannian geometry study of vapor-liquid phase equilibria and supercritical behavior of the Lennard-Jones fluid, *Phys. Rev. E* **85**, 031201 (2012).
- [15] J. Luo, L. Xu, E. Lascaris, H. E. Stanley, and S. V. Buldyrev, Behavior of the Widom line in critical phenomena, *Phys. Rev. Lett.* **112**, 135701 (2014).
- [16] D. T. Banuti, M. Raju, and M. Ihme, Similarity law for Widom lines and coexistence lines, *Phys. Rev. E* **95**, 052120 (2017).
- [17] D. Corradini, M. Rovere, and P. Gallo, The Widom line and dynamical crossover in supercritical water: Popular water models versus experiments, *J. Chem. Phys.* **143**, 10.1063/1.4930542 (2015).
- [18] P. Gallo, D. Corradini, and M. Rovere, Widom line and dynamical crossovers as routes to understand supercritical water, *Nat. Commun.* **5**, 10.1038/ncomms6806 (2014).
- [19] E. N. de Jesús, J. Torres-Arenas, and A. L. Benavides, Widom line of real substances, *J. Mol. Liq.* **322**, 114529 (2021).
- [20] V. V. Brazhkin, Y. D. Fomin, A. G. Lyapin, V. N. Ryzhov, and K. Trachenko, Two liquid states of matter: A dynamic line on a phase diagram, *Phys. Rev. E* **85**, 031203 (2012).
- [21] T. J. Yoon, M. Y. Ha, W. B. Lee, and Y.-W. Lee, “two-phase” thermodynamics of the Frenkel line, *The Journal of Physical Chemistry Letters* **9**, 4550 (2018).
- [22] V. V. Brazhkin, Y. D. Fomin, A. G. Lyapin, V. N. Ryzhov, E. N. Tsiok, and K. Trachenko, “liquid-gas” transition in the supercritical region: Fundamental changes in the particle dynamics, *Phys. Rev. Lett.* **111**, 145901 (2013).
- [23] D. Bolmatov, V. V. Brazhkin, and K. Trachenko, Thermodynamic behaviour of supercritical matter, *Nat. Commun.* **4**, 10.1038/ncomms3331 (2013).
- [24] D. Bolmatov, D. Zav’yalov, M. Gao, and M. Zhernenkov, Structural evolution of supercritical CO₂ across the Frenkel line, *The Journal of Physical Chemistry Letters* **5**, 2785 (2014).
- [25] C. Prescher, Y. D. Fomin, V. B. Prakapenka, J. Stefanski, K. Trachenko, and V. V. Brazhkin, Experimental evidence of the Frenkel line in supercritical neon, *Phys. Rev. B* **95**, 134114 (2017).
- [26] D. Bolmatov, M. Zhernenkov, D. Zav’yalov, S. N. Tkachev, A. Cunsolo, and Y. Q. Cai, The Frenkel line: a direct exper-

- imental evidence for the new thermodynamic boundary, *Sci. Rep.* **5**, [10.1038/srep15850](https://doi.org/10.1038/srep15850) (2015).
- [27] Y. D. Fomin, V. N. Ryzhov, E. N. Tsiok, J. E. Proctor, C. Prescher, V. B. Prakapenka, K. Trachenko, and V. V. Brazhkin, Dynamics, thermodynamics and structure of liquids and supercritical fluids: crossover at the Frenkel line, *J. Phys. Condens. Matter* **30**, 134003 (2018).
- [28] J. E. Proctor, C. G. Pruteanu, I. Morrison, I. F. Crowe, and J. S. Loveday, Transition from gas-like to liquid-like behavior in supercritical N_2 , *The Journal of Physical Chemistry Letters* **10**, 6584 (2019).
- [29] Y. D. Fomin, V. N. Ryzhov, E. N. Tsiok, and V. V. Brazhkin, Dynamical crossover line in supercritical water, *Sci. Rep.* **5**, [10.1038/srep14234](https://doi.org/10.1038/srep14234) (2015).
- [30] X. Li and Y. Jin, Thermodynamic crossovers in supercritical fluids, *Proc. Natl. Acad. Sci.* **121**, [10.1073/pnas.2400313121](https://doi.org/10.1073/pnas.2400313121) (2024).
- [31] G. Sordi, P. Sémon, K. Haule, and A.-M. S. Tremblay, Pseudogap temperature as a Widom line in doped Mott insulators, *Sci. Rep.* **2**, [10.1038/srep00547](https://doi.org/10.1038/srep00547) (2012).
- [32] G. Sordi, P. Sémon, K. Haule, and A.-M. S. Tremblay, c -axis resistivity, pseudogap, superconductivity, and Widom line in doped Mott insulators, *Phys. Rev. B* **87**, 041101 (2013).
- [33] J. Vučićević, H. Terletska, D. Tanasković, and V. Dobrosavljević, Finite-temperature crossover and the quantum Widom line near the Mott transition, *Phys. Rev. B* **88**, 075143 (2013).
- [34] P.-O. Downey, O. Gingras, J. Fournier, C.-D. Hébert, M. Charlebois, and A.-M. S. Tremblay, Mott transition, Widom line, and pseudogap in the half-filled triangular lattice Hubbard model, *Phys. Rev. B* **107**, 125159 (2023).
- [35] M. A. Halasz, A. D. Jackson, R. E. Shrock, M. A. Stephanov, and J. J. M. Verbaarschot, Phase diagram of QCD, *Phys. Rev. D* **58**, 096007 (1998).
- [36] M. A. Stephanov, QCD phase diagram and the critical point, *Int. J. Mod. Phys. A* **20**, 4387 (2005).
- [37] J. N. Guenther, Overview of the QCD phase diagram, *Eur. Phys. J. A* **57**, 136 (2021).
- [38] G. Sordi and A.-M. S. Tremblay, Introducing the concept of Widom line in the QCD phase diagram, [arXiv:2312.12401 \[hep-ph\]](https://arxiv.org/abs/2312.12401).
- [39] L. Carr, ed., *Understanding quantum phase transitions* (CRC Press, Boca Raton, 2011).
- [40] S. Sachdev, *Quantum phase transitions*, 2nd ed. (Cambridge University Press, Cambridge, 2015).
- [41] M. Continentino, *Quantum scaling in many-body systems*, 2nd ed. (Cambridge University Press, Cambridge, 2017).
- [42] R. Coldea, D. A. Tennant, E. M. Wheeler, E. Wawrzynska, D. Prabhakaran, M. Telling, K. Habicht, P. Smeibidl, and K. Kiefer, Quantum criticality in an Ising chain: Experimental evidence for emergent E_8 symmetry, *Science* **327**, 177 (2010).
- [43] A. W. Kinross, M. Fu, T. J. Munsie, H. A. Dabkowska, G. M. Luke, S. Sachdev, and T. Imai, Evolution of quantum fluctuations near the quantum critical point of the transverse field Ising chain system $CoNb_2O_6$, *Phys. Rev. X* **4**, 031008 (2014).
- [44] J. Wu, M. Kormos, and Q. Si, Finite-temperature spin dynamics in a perturbed quantum critical Ising chain with an E_8 symmetry, *Phys. Rev. Lett.* **113**, 247201 (2014).
- [45] T. Liang, S. M. Koohpayeh, J. W. Krizan, T. M. McQueen, R. J. Cava, and N. P. Ong, Heat capacity peak at the quantum critical point of the transverse Ising magnet $CoNb_2O_6$, *Nat. Comm.* **6**, 7611 (2015).
- [46] H. Zou, Y. Cui, X. Wang, Z. Zhang, J. Yang, G. Xu, A. Okutani, M. Hagiwara, M. Matsuda, G. Wang, G. Mussardo, K. Hódsági, M. Kormos, Z. He, S. Kimura, R. Yu, W. Yu, J. Ma, and J. Wu, E_8 spectra of quasi-one-dimensional antiferromagnet $BaCo_2V_2O_8$ under transverse field, *Phys. Rev. Lett.* **127**, 077201 (2021).
- [47] Y. Xu, L. S. Wang, Y. Y. Huang, J. M. Ni, C. C. Zhao, Y. F. Dai, B. Y. Pan, X. C. Hong, P. Chauhan, S. M. Koohpayeh, N. P. Armitage, and S. Y. Li, Quantum critical magnetic excitations in spin-1/2 and spin-1 chain systems, *Phys. Rev. X* **12**, 021020 (2022).
- [48] V. Zauner-Stauber, L. Vanderstraeten, M. T. Fishman, F. Verstraete, and J. Haegeman, Variational optimization algorithms for uniform matrix product states, *Physical Review B* **97**, 045145 (2018).
- [49] W. Li, S.-J. Ran, S.-S. Gong, Y. Zhao, B. Xi, F. Ye, and G. Su, Linearized tensor renormalization group algorithm for the calculation of thermodynamic properties of quantum lattice models, *Phys. Rev. Lett.* **106**, 127202 (2011).
- [50] Y.-L. Dong, L. Chen, Y.-J. Liu, and W. Li, Bilayer linearized tensor renormalization group approach for thermal tensor networks, *Phys. Rev. B* **95**, 144428 (2017).
- [51] S.-J. Gu, Fidelity approach to quantum phase transitions, *Int. J. Mod. Phys. B* **24**, 4371 (2010).
- [52] L. Amico, R. Fazio, A. Osterloh, and V. Vedral, Entanglement in many-body systems, *Rev. Mod. Phys.* **80**, 517 (2008).
- [53] A. F. Albuquerque, F. Alet, C. Sire, and S. Capponi, Quantum critical scaling of fidelity susceptibility, *Phys. Rev. B* **81**, 064418 (2010).
- [54] See Supplemental Material at [URL] for details on (i) supercritical scaling analysis, (ii) results for q -state quantum Potts model with a longitudinal field, (iii) implications of quantum supercriticality in Ising chain materials, which additionally includes Refs. [95–99].
- [55] P. Schauß, J. Zeiher, T. Fukuhara, S. Hild, M. Cheneau, T. Macrì, T. Pohl, I. Bloch, and C. Gross, Crystallization in Ising quantum magnets, *Science* **347**, 1455 (2015).
- [56] H. Labuhn, D. Barredo, S. Ravets, S. de Léséleuc, T. Macrì, T. Lahaye, and A. Browaeys, Tunable two-dimensional arrays of single Rydberg atoms for realizing quantum Ising models, *Nature* **534**, 667 (2016).
- [57] H. Bernien, S. Schwartz, A. Keesling, H. Levine, A. Omran, H. Pichler, S. Choi, A. S. Zibrov, M. Endres, M. Greiner, V. Vuletić, and M. D. Lukin, Probing many-body dynamics on a 51-atom quantum simulator, *Nature* **551**, 579 (2017).
- [58] E. Guardado-Sanchez, P. T. Brown, D. Mitra, T. Devakul, D. A. Huse, P. Schauß, and W. S. Bakr, Probing the quench dynamics of antiferromagnetic correlations in a 2d quantum Ising spin system, *Phys. Rev. X* **8**, 021069 (2018).
- [59] A. Omran, H. Levine, A. Keesling, G. Semeghini, T. T. Wang, S. Ebadi, H. Bernien, A. S. Zibrov, H. Pichler, S. Choi, J. Cui, M. Rossignolo, P. Rembold, S. Montangero, T. Calarco, M. Endres, M. Greiner, V. Vuletić, and M. D. Lukin, Generation and manipulation of Schrödinger cat states in Rydberg atom arrays, *Science* **365**, 570 (2019).
- [60] A. Keesling, A. Omran, H. Levine, H. Bernien, H. Pichler, S. Choi, R. Samajdar, S. Schwartz, P. Silvi, S. Sachdev, P. Zoller, M. Endres, M. Greiner, V. Vuletić, and M. D. Lukin, Quantum Kibble-Zurek mechanism and critical dynamics on a programmable Rydberg simulator, *Nature* **568**, 207 (2019).
- [61] D. Bluvstein, A. Omran, H. Levine, A. Keesling, G. Semeghini, S. Ebadi, T. T. Wang, A. A. Michailidis, N. Maskara, W. W. Ho, S. Choi, M. Serbyn, M. Greiner, V. Vuletić, and M. D. Lukin, Controlling quantum many-body dynamics in driven Rydberg atom arrays, *Science* **371**, 1355 (2021).
- [62] G. Semeghini, H. Levine, A. Keesling, S. Ebadi, T. T. Wang, D. Bluvstein, R. Verresen, H. Pichler, M. Kalinowski, R. Sama-

- jdard, A. Omran, S. Sachdev, A. Vishwanath, M. Greiner, V. Vuletić, and M. D. Lukin, Probing topological spin liquids on a programmable quantum simulator, *Science* **374**, 1242 (2021).
- [63] S. Ebadi, T. T. Wang, H. Levine, A. Keesling, G. Semeghini, A. Omran, D. Bluvstein, R. Samajdar, H. Pichler, W. W. Ho, S. Choi, S. Sachdev, M. Greiner, V. Vuletić, and M. D. Lukin, Quantum phases of matter on a 256-atom programmable quantum simulator, *Nature* **595**, 227 (2021).
- [64] P. Scholl, M. Schuler, H. J. Williams, A. A. Eberharter, D. Barredo, K.-N. Schymik, V. Lienhard, L.-P. Henry, T. C. Lang, T. Lahaye, A. M. Läuchli, and A. Browaeys, Quantum simulation of 2D antiferromagnets with hundreds of Rydberg atoms, *Nature* **595**, 233 (2021).
- [65] P. Schauss, Quantum simulation of transverse Ising models with Rydberg atoms, *Quantum Science and Technology* **3**, 023001 (2018).
- [66] A. Browaeys and T. Lahaye, Many-body physics with individually controlled Rydberg atoms, *Nat. Phys.* **16**, 132 (2020).
- [67] M. Morgado and S. Whitlock, Quantum simulation and computing with Rydberg-interacting qubits, *AVS Quantum Science* **3**, 10.1116/5.0036562 (2021).
- [68] X. Wu, X. Liang, Y. Tian, F. Yang, C. Chen, Y.-C. Liu, M. K. Tey, and L. You, A concise review of Rydberg atom based quantum computation and quantum simulation, *Chinese Physics B* **30**, 020305 (2021).
- [69] S. R. White, Density matrix formulation for quantum renormalization groups, *Phys. Rev. Lett.* **69**, 2863 (1992).
- [70] U. Schollwöck, The density-matrix renormalization group in the age of matrix product states, *Annals of Physics* **326**, 96 (2011).
- [71] M. Fishman, S. White, and E. Stoudenmire, The ITensor software library for tensor network calculations, *SciPost Physics Codebases* 10.21468/scipostphyscodeb.4 (2022).
- [72] M. E. Fisher, S.-k. Ma, and B. G. Nickel, Critical exponents for long-range interactions, *Phys. Rev. Lett.* **29**, 917 (1972).
- [73] M. Knap, A. Kantian, T. Giamarchi, I. Bloch, M. D. Lukin, and E. Demler, Probing real-space and time-resolved correlation functions with many-body Ramsey interferometry, *Phys. Rev. Lett.* **111**, 147205 (2013).
- [74] S. Fey and K. P. Schmidt, Critical behavior of quantum magnets with long-range interactions in the thermodynamic limit, *Phys. Rev. B* **94**, 075156 (2016).
- [75] N. Defenu, A. Trombettoni, and S. Ruffo, Criticality and phase diagram of quantum long-range $O(N)$ models, *Phys. Rev. B* **96**, 104432 (2017).
- [76] S. L. Sondhi, S. M. Girvin, J. P. Carini, and D. Shahar, Continuous quantum phase transitions, *Rev. Mod. Phys.* **69**, 315 (1997).
- [77] I. Frérot and T. Roscilde, Reconstructing the quantum critical fan of strongly correlated systems using quantum correlations, *Nat. Commun.* **10**, 10.1038/s41467-019-08324-9 (2019).
- [78] C. M. Morris, R. Valdés Aguilar, A. Ghosh, S. M. Koohpayeh, J. Krizan, R. J. Cava, O. Tchernyshyov, T. M. McQueen, and N. P. Armitage, Hierarchy of bound states in the one-dimensional ferromagnetic Ising chain CoNb_2O_6 investigated by high-resolution time-domain terahertz spectroscopy, *Phys. Rev. Lett.* **112**, 137403 (2014).
- [79] I. Cabrera, J. D. Thompson, R. Coldea, D. Prabhakaran, R. I. Bewley, T. Guidi, J. A. Rodriguez-Rivera, and C. Stock, Excitations in the quantum paramagnetic phase of the quasi-one-dimensional Ising magnet CoNb_2O_6 in a transverse field: Geometric frustration and quantum renormalization effects, *Phys. Rev. B* **90**, 014418 (2014).
- [80] K. Matsuura, P. T. Cong, S. Zherlitsyn, J. Wosnitza, N. Abe, and T.-h. Arima, Anomalous lattice softening near a quantum critical point in a transverse Ising magnet, *Phys. Rev. Lett.* **124**, 127205 (2020).
- [81] K. Amelin, J. Engelmayer, J. Viirik, U. Nagel, T. Rõ om, T. Lorenz, and Z. Wang, Experimental observation of quantum many-body excitations of E_8 symmetry in the Ising chain ferromagnet CoNb_2O_6 , *Phys. Rev. B* **102**, 104431 (2020).
- [82] M. Fava, R. Coldea, and S. A. Parameswaran, Glide symmetry breaking and Ising criticality in the quasi-1D magnet CoNb_2O_6 , *Proc. Natl. Acad. Sci.* **117**, 25219 (2020).
- [83] C. M. Morris, N. Desai, J. Viirik, D. Hüvonen, U. Nagel, T. Rõ om, J. W. Krizan, R. J. Cava, T. M. McQueen, S. M. Koohpayeh, R. K. Kaul, and N. P. Armitage, Duality and domain wall dynamics in a twisted Kitaev chain, *Nat. Phys.* **17**, 832 (2021).
- [84] L. Woodland, D. Macdougall, I. M. Cabrera, J. D. Thompson, D. Prabhakaran, R. I. Bewley, and R. Coldea, Tuning the confinement potential between spinons in the Ising chain CoNb_2O_6 using longitudinal fields and quantitative determination of the microscopic hamiltonian, *Phys. Rev. B* **108**, 184416 (2023).
- [85] Q. Faure, S. Takayoshi, S. Petit, V. Simonet, S. Raymond, L.-P. Regnault, M. Boehm, J. S. White, M. Månsson, C. Rüegg, P. Lejay, B. Canals, T. Lorenz, S. C. Furuya, T. Giamarchi, and B. Grenier, Topological quantum phase transition in the Ising-like antiferromagnetic spin chain $\text{BaCo}_2\text{V}_2\text{O}_8$, *Nat. Phys.* **14**, 716 (2018).
- [86] Z. Wang, T. Lorenz, D. I. Gorbunov, P. T. Cong, Y. Kohama, S. Niesen, O. Breunig, J. Engelmayer, A. Herman, J. Wu, K. Kindo, J. Wosnitza, S. Zherlitsyn, and A. Loidl, Quantum criticality of an Ising-like spin-1/2 antiferromagnetic chain in a transverse magnetic field, *Phys. Rev. Lett.* **120**, 207205 (2018).
- [87] Z. Wang, M. Schmidt, A. Loidl, J. Wu, H. Zou, W. Yang, C. Dong, Y. Kohama, K. Kindo, D. I. Gorbunov, S. Niesen, O. Breunig, J. Engelmayer, and T. Lorenz, Quantum critical dynamics of a Heisenberg-Ising chain in a longitudinal field: Many-body strings versus fractional excitations, *Phys. Rev. Lett.* **123**, 067202 (2019).
- [88] Z. Zhang, K. Amelin, X. Wang, H. Zou, J. Yang, U. Nagel, T. Rõ om, T. Dey, A. A. Nugroho, T. Lorenz, J. Wu, and Z. Wang, Observation of E_8 particles in an Ising chain antiferromagnet, *Phys. Rev. B* **101**, 220411 (2020).
- [89] A. Okutani, T. Kida, T. Usui, T. Kimura, K. Okunishi, and M. Hagiwara, High field magnetization of single crystals of the $S = 1/2$ quasi-1D Ising-like antiferromagnet $\text{SrCo}_2\text{V}_2\text{O}_8$, *Physics Procedia* **75**, 779 (2015).
- [90] Z. Wang, J. Wu, W. Yang, A. K. Bera, D. Kamenskyi, A. T. M. N. Islam, S. Xu, J. M. Law, B. Lake, C. Wu, and A. Loidl, Experimental observation of Bethe strings, *Nature* **554**, 219 (2018).
- [91] Y. Cui, H. Zou, N. Xi, Z. He, Y. X. Yang, L. Shu, G. H. Zhang, Z. Hu, T. Chen, R. Yu, J. Wu, and W. Yu, Quantum criticality of the Ising-like screw chain antiferromagnet $\text{SrCo}_2\text{V}_2\text{O}_8$ in a transverse magnetic field, *Phys. Rev. Lett.* **123**, 067203 (2019).
- [92] S. T. Carr and A. M. Tsvelik, Spectrum and correlation functions of a quasi-one-dimensional quantum Ising model, *Phys. Rev. Lett.* **90**, 177206 (2003).
- [93] K. Okunishi and T. Suzuki, Field-induced incommensurate order for the quasi-one-dimensional XXZ model in a magnetic field, *Phys. Rev. B* **76**, 224411 (2007).
- [94] C. Sheng, J. Hou, X. He, P. Xu, K. Wang, J. Zhuang, X. Li, M. Liu, J. Wang, and M. Zhan, Efficient preparation of two-dimensional defect-free atom arrays with near-fewest sorting-atom moves, *Phys. Rev. Res.* **3**, 023008 (2021).
- [95] J. Sólyom and P. Pfeuty, Renormalization-group study of the Hamiltonian version of the Potts model, *Phys. Rev. B* **24**, 218 (1981).

- [96] A. Rapp and G. Zaránd, Dynamical correlations and quantum phase transition in the quantum Potts model, *Phys. Rev. B* **74**, 014433 (2006).
- [97] M. Campostrini, J. Nespolo, A. Pelissetto, and E. Vicari, Finite-size scaling at the first-order quantum transitions of quantum Potts chains, *Phys. Rev. E* **91**, 052103 (2015).
- [98] C. Ding, Y. Wang, Y. Deng, and H. Shao, Monte Carlo simulation of quantum Potts model, [arXiv:1702.02675](https://arxiv.org/abs/1702.02675) [*cond-mat.stat-mech*].
- [99] C. Karrasch and D. Schuricht, Dynamical quantum phase transitions in the quantum Potts chain, *Phys. Rev. B* **95**, 075143 (2017).

Supplemental Materials for: Quantum Supercriticality in the Ising Model and Rydberg Atom Array

A. DERIVATION OF THE SUPERCRITICAL SCALING RELATIONS

Magnetic susceptibility χ_z .— The starting point is the singular part of the ground-state energy \mathcal{U} near the quantum critical point (QCP), which reads [41]

$$\mathcal{U} = \tilde{h}_x^{2-\alpha} \phi_E(x) \quad (\text{A1})$$

where $x \equiv h_z / \tilde{h}_x^{\beta+\gamma}$.

In the quantum supercritical (QSC) regime, the ground-state energy is symmetric around $h_z = 0$. Consequently, we can perform a Taylor expansion of the scaling function $\phi_E(x)$ near $x = 0$, retaining only the even-order terms.

$$\phi_E(x) = \sum_{n=0,2,4,\dots} \frac{\phi_E^{(n)}(0)}{n!} x^n \quad (\text{A2})$$

The singular magnetic susceptibility \mathcal{X}_z is obtained as

$$\mathcal{X}_z = -\frac{\partial^2 \mathcal{U}}{\partial h_z^2} = -\tilde{h}_x^{2-\alpha-2(\beta+\gamma)} \phi_E''(x). \quad (\text{A3})$$

Using the Rushbrooke relation $\alpha + 2\beta + \gamma = 2$, one arrives at

$$\mathcal{X}_z = \tilde{h}_x^{-\gamma} \phi_{\chi_z}(x) \quad (\text{A4})$$

with $\phi_{\chi_z}(x) \equiv -\phi_E''(x)$. To derive the scaling behavior of the QSC crossover line, note that from Eq. (A4) we have

$$\mathcal{X}_z = h_z^{-\frac{\gamma}{\beta+\gamma}} \tilde{\phi}_{\chi_z}(x) \quad (\text{A5})$$

with $\tilde{\phi}_{\chi_z}(x) \equiv x^{\frac{\gamma}{\beta+\gamma}} \phi_{\chi_z}(x)$. Then, the peak position of magnetic susceptibility can be determined as $x = x_0$, i.e., $h_z = x_0 \cdot \tilde{h}_x^{\beta+\gamma}$, where $\tilde{\phi}_{\chi_z}(x_0) = 0$. The scaling functions $\phi_{\chi_z}(x)$ [Eq. (A4)] and $\tilde{\phi}_{\chi_z}(x)$ [Eq. (A5)] obtained by data collapse are shown in Fig. 3 of the main text. As the scaling function $\phi_E(x)$ is of parity even, we expand $\phi_{\chi_z}(x)$ as follows

$$\phi_{\chi_z}(x) = -\phi_E''(x) = -\phi_E''(0) - \frac{1}{2} \phi_E^{(4)}(0) x^2 + \mathcal{O}(x^4) \quad (\text{A6})$$

which is nearly a constant function in QSC regime.

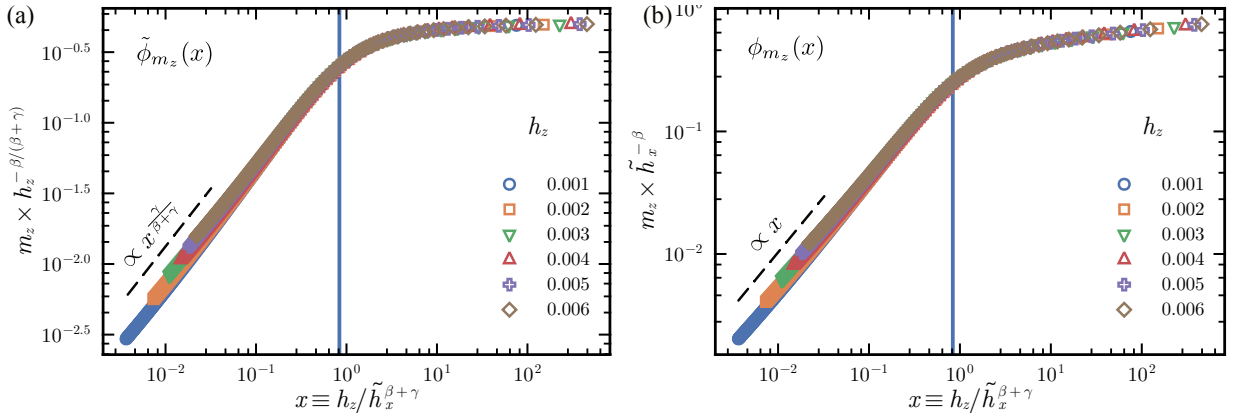


FIG. S1. Scaling functions (a) $\tilde{\phi}_{m_z}(x)$ and (b) $\phi_{m_z}(x)$ obtained via data collapse from the calculated magnetization m_z , based on Eqs. (A7) and (A8). The vertical blue line $x = x_0$ is determined from the magnetic susceptibility χ_z in the main text.

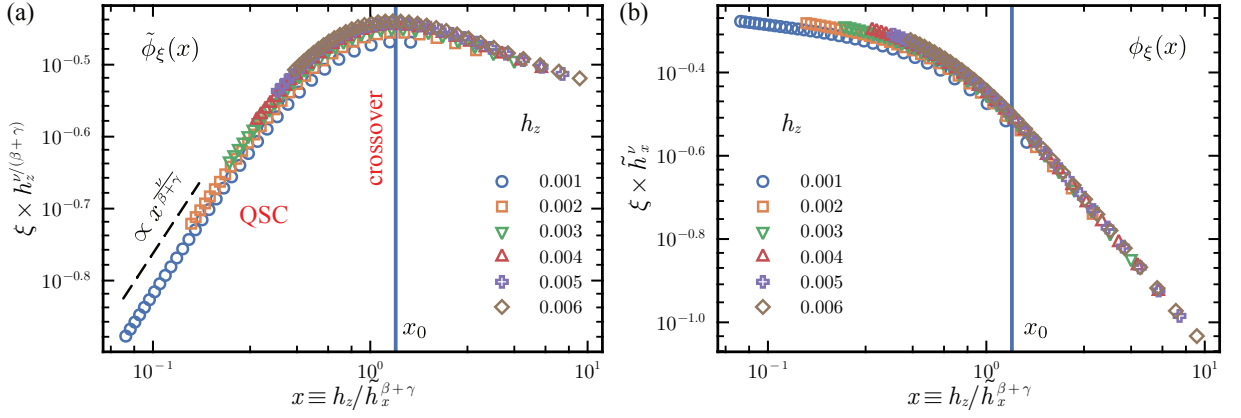


FIG. S2. Scaling functions (a) $\tilde{\phi}_\xi(x)$ and (b) $\phi_\xi(x)$ are obtained via data collapse of the calculated correlation length ξ , according to Eqs. (A9) and (A10). The vertical blue line, which corresponds to $\tilde{\phi}'_\xi(x_0) = 0$, is derived from Fig. 2(c) of the main text. This line accurately marks the peak of the scaling function $\tilde{\phi}_\xi(x)$.

Within the supercritical regime ($x \lesssim x_0$), the scaling function is nearly a constant function $\phi_{\chi_z}(x) \approx \phi_{\chi_z}(0)$ [as numerically shown in the left top part of Fig. 3(b) in the main text] and it thus arrives at $\chi_z \sim \tilde{h}_x^{-\gamma}$ in the QSC regime. In the vicinity of the crossover line, $\phi_{\chi_z}(x)$ ceases to be a slowly varying function, and as a result, χ_z will deviate from the universal scaling form.

Magnetization m_z .— From Eq. (A1), the singular part of magnetization along z direction reads

$$\begin{aligned} \mathcal{M}_z &= -\frac{\partial \mathcal{U}}{\partial h_z} = -\tilde{h}_x^{2-\alpha-(\beta+\gamma)} \phi'_E(x) \\ &= \tilde{h}_x^\beta \phi_{m_z}(x), \end{aligned} \quad (\text{A7})$$

with $\phi_{m_z}(x) \equiv -\phi'_E(x) = -\phi''_E(0)x + \mathcal{O}(x^3)$. Then it follows that along the $h_z \propto \tilde{h}_x^{\beta+\gamma}$ line where $x = \text{const.}$, $\phi_{m_z}(x)$ becomes a constant, and we have $m_z \propto \tilde{h}_x^\beta$. Note that based on Eq. (A7), we also have

$$\mathcal{M}_z = h_z^{\frac{\beta}{\beta+\gamma}} \tilde{\phi}_{m_z}(x), \quad (\text{A8})$$

where $\tilde{\phi}_{m_z}(x) = x^{-\frac{\beta}{\beta+\gamma}} \phi_{m_z}(x)$. The scaling functions $\tilde{\phi}_{m_z}(x)$ and $\phi_{m_z}(x)$ are obtained by data collapse, according to Eq. (A7) and Eq. (A8), are shown in Fig. S1.

Correlation length ξ .— For the singular part of the correlation length \mathcal{L} near QCP, we similarly have [41]

$$\mathcal{L} = \tilde{h}_x^{-\nu} \phi_\xi(x). \quad (\text{A9})$$

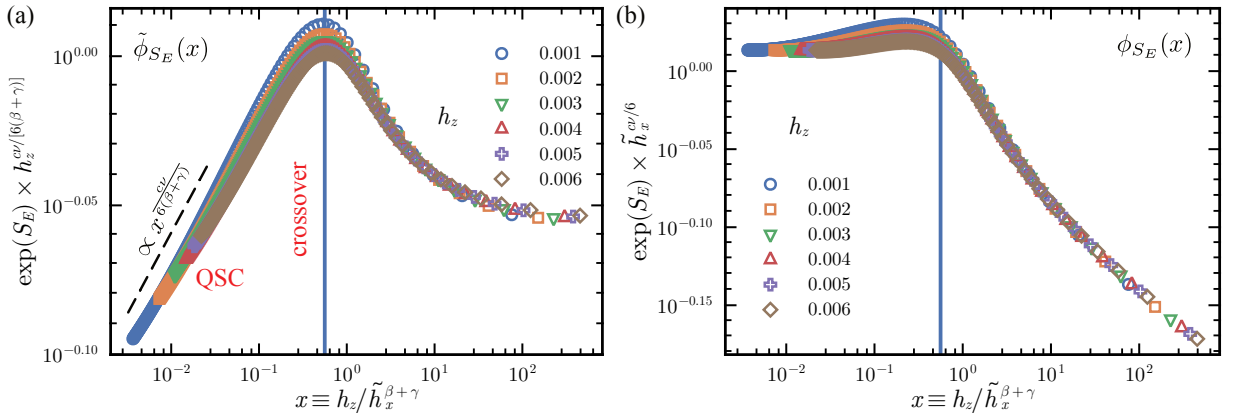


FIG. S3. Scaling functions (a) $\tilde{\phi}_{S_E}(x)$ and (b) $\phi_{S_E}(x)$ obtained via the data collapse of the calculated entanglement entropy S_E , according to Eqs. (A12) and (A13). The vertical blue line is determined from Fig. 2(d) of the main text.

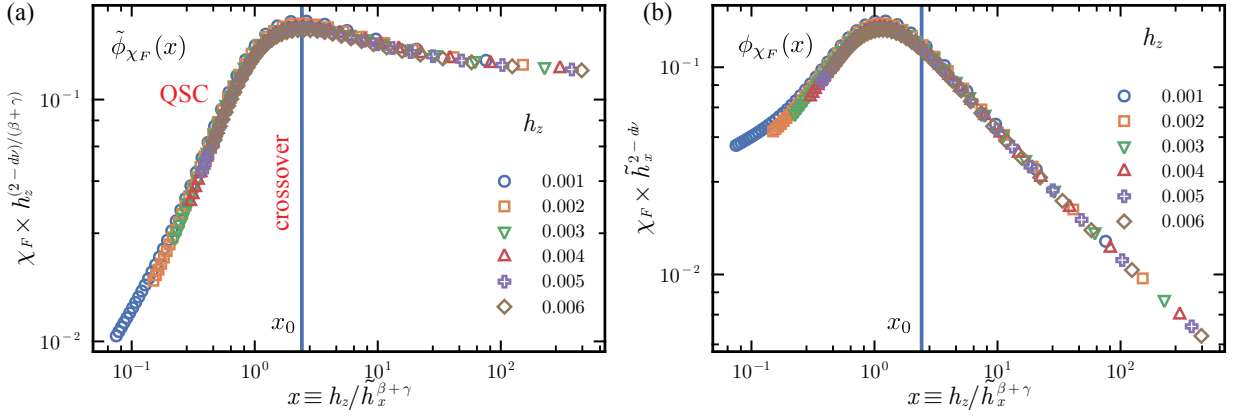


FIG. S4. Scaling functions (a) $\tilde{\phi}_{\chi_F}(x)$ and (b) $\phi_{\chi_F}(x)$ obtained via data collapse of the calculated fidelity susceptibility χ_F , based on Eqs. (A14) and (A15). The blue vertical line, which corresponds to $\tilde{\phi}'_{\chi_F}(x_0) = 0$, is derived from Fig. 2(e) in the main text. This line also locates precisely at the peak of the scaling function $\tilde{\phi}_{\chi_F}(x)$.

To derive the scaling behavior of the QSC crossover line, note that from Eq. (A9) we have

$$\mathcal{Z} = h_z^{-\frac{\nu}{\beta+\gamma}} \tilde{\phi}_\xi(x), \quad (\text{A10})$$

with $\tilde{\phi}_\xi(x) \equiv x^{\frac{\nu}{\beta+\gamma}} \phi_\xi(x)$. Therefore, the peak position of ξ for a fixed h_z is obtained by $\tilde{\phi}'_\xi(x_0) = 0$, which leads to $h_z = x_0 \cdot \tilde{h}_x^{\beta+\gamma}$ forming the QSC crossover line. We show the scaling functions in Fig. S2 through data collapse following Eq. (A9) and Eq. (A10). Then, we expand the scaling function $\phi_\xi(x)$ as

$$\phi_\xi(x) = \sum_{n=0,2,4,\dots} \frac{\phi_\xi^{(n)}(0)}{n!} x^n, \quad (\text{A11})$$

and find that the scaling relation $\xi \sim \tilde{h}_x^{-\nu}$ holds in the QSC regime as $\phi_\xi(x) \approx \phi_\xi(0)$.

Entanglement entropy S_E .— The scaling relation of entanglement entropy S_E and its corresponding QSC crossover line can be obtained based on the scaling relation $S_E \sim \frac{c\nu}{6} \ln(\xi)$ near QCP [52]. As $\xi \sim \tilde{h}_x^{-\nu}$, we conjecture that the singular part of the entanglement entropy \mathcal{S}_E satisfies $\mathcal{S}_E \sim -\frac{c\nu}{6} \ln(\tilde{h}_x) \phi_{S_E}(x)$, which we formally rewrite as

$$\exp(\mathcal{S}_E) = \tilde{h}_x^{-\frac{c\nu}{6}} \phi_{S_E}(x), \quad (\text{A12})$$

with an equivalent expression

$$\exp(\mathcal{S}_E) = h_z^{-\frac{c\nu}{6(\beta+\gamma)}} \tilde{\phi}_{S_E}(x), \quad (\text{A13})$$

where $\tilde{\phi}_{S_E}(x) \equiv x^{\frac{c\nu}{6(\beta+\gamma)}} \phi_{S_E}(x)$. In Fig. S3, we present the two scaling functions $\phi_{S_E}(x)$ and $\tilde{\phi}_{S_E}(x)$ through data collapse for S_E based on Eqs. (A12) and (A13). We expand $\phi_{S_E}(x)$ and retain the zero-th order term $\phi_{S_E}(0)$ that dominates in the QSC regime, and find $S_E \sim \frac{c\nu}{6} \ln \tilde{h}_x$ from Eq. (A12), which has been observed in Fig. 2(d) of the main text.

Fidelity susceptibility χ_F .— For the fidelity susceptibility, from the discussions given in Ref. [53], we conjecture the singular part of χ_F falls into the universal form

$$\mathcal{Z}_F = \tilde{h}_x^{d\nu-2} \phi_{\chi_F}(x) \quad (\text{A14})$$

To derive the scaling behaviors, note that from Eq. (A14) we have

$$\mathcal{Z}_F = h_z^{\frac{d\nu-2}{\beta+\gamma}} \tilde{\phi}_{\chi_F}(x) \quad (\text{A15})$$

with $\tilde{\phi}_{\chi_F}(x) = x^{\frac{2-d\nu}{\beta+\gamma}} \phi_{\chi_F}(x)$. Thus, the peak position x_0 of χ_F for a fixed h_z can be determined by solving $\tilde{\phi}'_{\chi_F}(x_0) = 0$. This condition results in $h_z = x_0 \cdot \tilde{h}_x^{\beta+\gamma}$, which once more defines the QSC crossover line. The scaling functions $\phi_{\chi_F}(x)$ and $\tilde{\phi}_{\chi_F}(x)$ are obtained via data collapse in Fig. S4, based on Eq. (A14) and Eq. (A15), respectively. Hence the scaling relation $\chi_F \sim \tilde{h}_x^{d\nu-2}$ holds as $\phi_{\chi_F}(x) \approx \phi_{\chi_F}(0)$ in the QSC regime with small x values.

B. q -STATE QUANTUM POTTS MODEL WITH A LONGITUDINAL FIELD

Here we affirm the universal scalings associated with the QSC regime by studying a generalization of transverse field Ising chain, namely the q -state (for $q=3$ and 4) quantum Potts chain with a longitudinal field, whose Hamiltonian reads [95–99]

$$H/J = - \sum_i \left(\sum_{\mu=1}^q P_i^\mu P_{i+1}^\mu \right) - g \sum_i P_i - h \sum_i \left(\sum_{\mu=1}^q \frac{1}{\mu} P_i^\mu \right). \quad (\text{B16})$$

Here the traceless operators $P_i^\mu = |\mu\rangle\langle\mu| - 1/q$ tend to project the spin at site i along the direction μ , and thus the first term promotes a “ferromagnetic” ground state. While g term represents a transverse field with the traceless operator $P_i = |\lambda\rangle\langle\lambda| - 1/q$ trying to align the spins along the direction $|\lambda\rangle = \sum_{\mu} |\mu\rangle / \sqrt{q}$. The h term represents one type of longitudinal field, which explicitly breaks the permutation symmetry S_q and selects the first direction $\mu = 1$ among q possible ones. The phase diagram of this model resembles that of the Ising chain with a longitudinal field, with the critical point being at $g = g_c \equiv 1$ and $h = 0$, and we define $\tilde{g} = g - g_c$.

In the following calculations, we use variational uniform matrix product state algorithm and fix the maximal bond dimension to be $D = 256$. The numerical results for correlation length ξ for $q = 3$ and $q = 4$ are given in Fig. S5(a) and (b). The red lines, corresponding to $h = 0$, again show the scaling relation $\xi \sim \tilde{g}^{-\nu}$, where $\nu = 5/6$ and $3/2$, for $q = 3$ and $q = 4$, respectively. It is found that curves with $h \neq 0$ initially follow this same scaling law, but for \tilde{g} becoming small enough, they deviate. We extract the peaks from each curves, and present them in the $\ln h$ - $\ln \tilde{g}$ plane in the inset, which fit pretty well with the $\beta + \gamma$ power-law scaling as shown by the blue line. Similarly, we also give the numerical results for entanglement entropy for $q = 3$ and $q = 4$

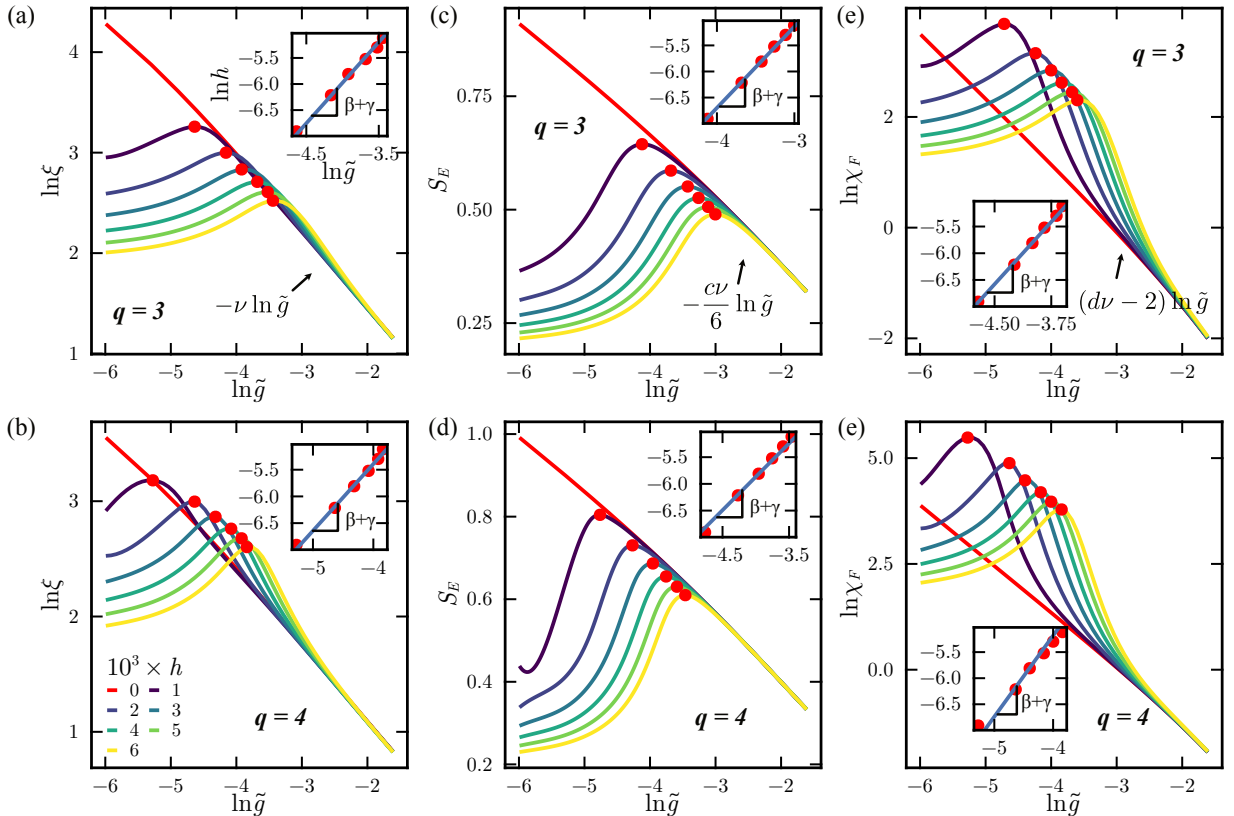


FIG. S5. Universal scalings and quantum supercritical crossovers for the q -state quantum Potts chain with a longitudinal field. (a) and (b) show the behavior of maximal correlation length for $q = 3$ and $q = 4$, respectively. The red lines with $h_z = 0$ show a scaling relation $\xi \sim \tilde{g}^{-\nu}$, where $\nu = 5/6$ and $3/2$, respectively. In the inset, we plot the peaks (red dots) obtained from these curves in the $\ln h$ - $\ln \tilde{g}$ plane, and they follow a power-law scaling $h \propto \tilde{g}^{\beta+\gamma}$ as given by the blue lines, where $\beta + \gamma = 1/9 + 13/9 = 14/9$ and $1/12 + 7/6 = 5/4$. (c) and (d) show the behavior of entanglement entropy S_E for $q = 3$ and $q = 4$, and the red lines with $h = 0$ show a critical scaling $S_E \sim -\frac{c\nu}{6} \ln \tilde{g}$, where $c = 4/5$ and 1, respectively. The same $\beta + \gamma$ power-law scalings for the supercritical crossover lines are also evident in the insets. (e) and (f) shows the behavior of fidelity susceptibility χ_F for $q = 3$ and $q = 4$, respectively. The red lines with $h = 0$ show a critical scaling $\chi_F \sim \tilde{g}^{d\nu-2}$, where $d = 1$ is the dimension of the system. The same $\beta + \gamma$ power-law scaling are also evident in the insets of (e) and (f).

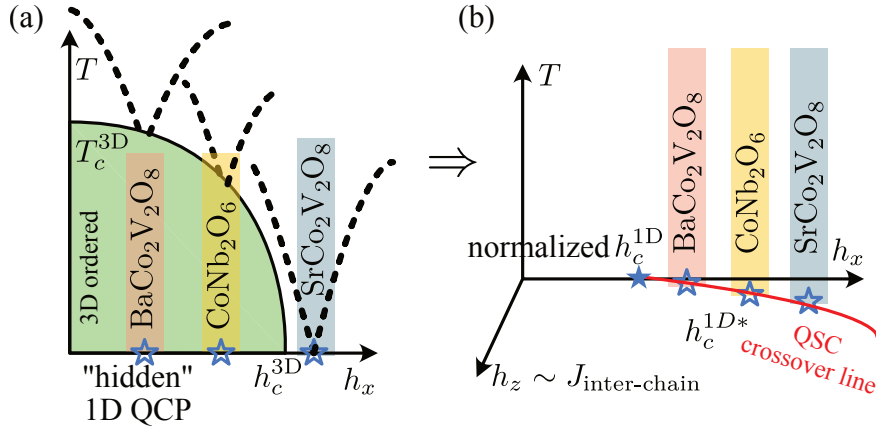


FIG. S6. (a) and (b) show a schematic illustration of quantum supercriticality in Ising chain materials. Due to mean-field interchain coupling, there is a small effective longitudinal field. Hence the experimentally observed “hidden” 1D QCP are actually replaced by pseudo QCPs (hollow stars) sitting on the QSC crossover line. The relative position between these pseudo QCPs and the 3D QCP is effectively controlled by this longitudinal field.

in Fig. S5(c) and (d). The red lines, corresponding to $h = 0$, show the scaling relation $S_E \sim -\frac{c\nu}{6} \ln \tilde{g}$ [52], where $c = 4/5$ and 1, for $q = 3$ and $q = 4$, respectively. It is found that again the curves with nonzero h initially follow this same scaling, but eventually deviate as g close to g_c , and the entanglement is larger in the supercritical regime. The $q = 4$ case shows a sharper and higher peak than the $q = 3$ case. We also collect all these peaks from each curves and present them in the inset, which constitute a QSC crossover line and fit pretty well with $h \sim \tilde{g}^{\beta+\gamma}$ power-law scaling as shown by the blue line in the insets.

Lastly, in Fig. S5(e) and (f) we show the calculated results of fidelity susceptibility for the $q = 3$ and $q = 4$ cases. The red line, corresponding to $h = 0$, show a scaling relation $\chi_F \sim \tilde{g}^{d\nu-2}$ [53], where $d = 1$ is the dimension of the system. It is found that again the curves with nonzero h initially follow this same scaling, but eventually deviate as g approaching g_c . We also extract all these peaks from each curve and present them in the inset, and again arrive at the QSC crossover line $h \sim \tilde{g}^{\beta+\gamma}$. Note here $\beta + \gamma = 1/9 + 13/9 = 14/9$ for $q = 3$, and $\beta + \gamma = 1/12 + 7/6 = 5/4$ for $q = 4$, according to the 3- and 4-state Potts universality class.

C. QUANTUM SUPERCRITICALITY AND PSEUDO QCP IN COUPLED ISING CHAIN MATERIALS

Recently, there is a plethora of studies on quantum Ising chain materials like CoNb_2O_6 [42–45, 47, 78–84], $\text{BaCo}_2\text{V}_2\text{O}_8$ [46, 85–88], and $\text{SrCo}_2\text{V}_2\text{O}_8$ [89–91], where 1D quantum critical fans are observed experimentally [dubbed as “hidden” QCP in certain literature, c.f., Fig. S6(a)]

Since inter-chain coupling in these materials is much smaller than the intrachain coupling, they can be well approximated by weakly coupled, transverse field Ising chains. In addition, a small longitudinal field is inevitable: the interchain mean-field approximation will provide an effective longitudinal field in the mean-field level [92, 93]. Hence, this longitudinal field turns the QCP into a smooth QSC crossover, or, more precisely a pseudo QCP of h^* sitting on a QSC crossover line $h_z \sim (h^* - h_c)^{\beta+\gamma}$ [see Fig. S6(b)]. The pseudo QCP significantly impacts the low-temperature properties of the system, functioning as a “hidden” 1D QCP. Different compounds may have different effective longitudinal fields h_z and the pseudo QCP shifts along the QSC crossover line as illustrated in Fig. S6.